Misfit-energy-increasing dislocations in vapor-deposited CoFe/NiFe multilayers

X. W. Zhou, R. A. Johnson, and H. N. G. Wadley
Department of Materials Science and Engineering, School of Engineering and Applied Science, University of Virginia, Charlottesville, Virginia 22903, USA

(Received 14 May 2003; revised manuscript received 29 September 2003; published 20 April 2004)

Recent molecular dynamics simulations of the growth of $[Ni_{0.8}Fe_{0.2}/Au]$ multilayers have revealed the formation of misfit-strain-reducing dislocation structures very similar to those observed experimentally. Here we report similar simulations showing the formation of edge dislocations near the interfaces of vapor-deposited (111) [NiFe/CoFe/Cu] multilayers. Unlike misfit dislocations that accommodate lattice mismatch, the dislocation structures observed here increase the mismatch strain energy. Stop-action observations of the dynamically evolving atomic structures indicate that during deposition on the (111) surface of a fcc lattice, adatoms may occupy either fcc sites or hcp sites. This results in the random formation of fcc and hcp domains, with dislocations at the domain boundaries. These dislocations enable atoms to undergo a shift from fcc to hcp sites, or vice versa. These shifts lead to missing atoms, and therefore a later deposited layer can have missing planes compared to a previously deposited layer. This dislocation formation mechanism can create tensile stress in fcc films. The probability that such dislocations are formed was found to quickly diminish under energetic deposition conditions.

DOI: 10.1103/PhysRevB.69.144113 PACS number(s): 61.72.Lk, 68.65.Ac, 61.72.Bb, 61.43.Bn

I. INTRODUCTION

Multilayer structures composed of thin (~30–50 Å) ferromagnetic metal layers (nickel, iron, cobalt, or their alloys) separated by thin (~20 Å) conductive spacer layers (copper or copper alloys) exhibit giant magnetoresistance (GMR).[1] Due to an oscillatory exchange interaction that propagates through the nonmagnetic spacer layer, antiparallel alignment of the magnetic moments of the layers on both sides of the spacer layer occurs at certain discrete spacer layer thicknesses.[2] At these discrete spacer layer thicknesses, the antiferromagnetically aligned multilayers exhibit a relatively high electrical resistance because electrons with any spin scatter off one or other of the spacer/magnetic layer interfaces. When an external magnetic field brings the magnetic moments of the ferromagnetic layers into parallel alignment, less scattering will occur for at least half of the electrons (if the spin directions of electrons are equally divided). The material then has a relatively low electrical resistance.

GMR multilayers of this type must have a uniform spacer thickness to result in ideal magnetic coupling.[3] Interdiffusion between adjacent layers needs to be avoided. For example, if nickel atoms diffuse into the copper spacer layer (or vice versa), the magnetic moment alignment of the nickel is locally lost, creating a magnetic dead zone.[4] These mixed atoms also become centers for spin-independent scattering that reduces the GMR ratio.[5] Iron or cobalt atoms that diffuse into copper can have an even worse effect because they will maintain their moments and cause spin-flip scattering.[5] To achieve the full potential of these structures, the multilayers must have atomically smooth chemically separated interfaces. They also need to contain a minimum of other electron scattering structural defects.[5–7]

The growth of nanoscale multilayers often introduces significant stresses and dislocation densities due to the lattice mismatch between the different layers.[8] Little attention has been paid to these dislocations in GMR multilayers, even though their existence may have significant consequences for magnetotransport. First, stresses and dislocations are interrelated and often interact to affect the growth mode. Examples include the spiral growth along a screw-type dislocation normal to the growth surface[9] and stress-driven surface roughening.[10] Because dislocations can pin the motion of magnetic domain walls,[11] they can directly affect GMR effects. Magnetoelastic effects can also be important if large stresses exist in the layers. It should be realized that the motion of a dislocation across an interface can cause an atomic step to form on the interface. This is equivalent to an increase in atomic roughness.

The formation of misfit dislocations during the epitaxial growth of films has been extensively investigated using a continuum mechanics approach.[8,12,13] When a crystalline film is epitaxially deposited on a crystalline substrate, differences in the lattice parameters of the deposited film and the substrate can be accommodated by an elastic strain. For significant lattice mismatches, this elastic strain results in a large biaxial stress in the deposited film. As the film thickness increases, the elastic strain energy becomes larger, and at a critical film thickness the system energy can be reduced by introducing misfit (edge) dislocations.[8] These misfit dislocations, when aligned along the substrate/deposit interface, create extra planes and increase the lateral dimension of the layer with the smaller lattice parameter. This provides a mechanism to accommodate the misfit strain and reduce the misfit stress. Misfit dislocations can form immediately upon vapor deposition, or they can be introduced by plastic flow after a certain thickness of the layer has been deposited. An equilibrium theory of misfit dislocations in thin films was first proposed by van der Merwe in the 1960s,[14] and has since been significantly embellished.[15–27] These theories established both the equilibrium configurations of misfit dislocations and their formation mechanisms. However, they do not address the nonequilibrium dislocations that can be incorporated during film growth because of kinetic constraints

upon the atomic assembly processes.

In a continuum mechanics, a crystal lattice is coarse grained into an equivalent continuum medium. Such an approach is unable to address the complex atomic assembly processes during deposition of a thin film. Densities of defects such as vacancies, stacking faults, and dislocations can be significantly different from those predicted by equilibrium theories when insufficient time is available to ''equilibrate'' the local structure as deposition progresses.[12,28,29] The defect density is highly sensitive to the precise details of the various atomic assembly events.[30–34] For GMR systems of interest here, it is now possible to realistically simulate the dislocation formation mechanisms during kinetically constrained crystal growth using atomistic simulation approaches. A molecular dynamics simulation has recently been used to simulate the growth of $Au/Ni_{0.8}Fe_{0.2}$ multilayers.[35] The approach predicted the formation of misfit dislocations on both the Au-on-$Ni_{0.8}Fe_{0.2}$ and the $Ni_{0.8}Fe_{0.2}$-on-Au interfaces. The dislocation type and spacing were found to be in good agreement with experimental observations.[36] The study also provided more insights into the atomistic origins of misfit dislocation nucleation. $Au/Ni_{0.8}Fe_{0.2}$ multilayers are an example of a system with a very large lattice mismatch ($\sim$15%), which promotes the direct formation of misfit dislocations at interfaces during vapor deposition. For systems with a lower lattice mismatch grown under kinetically constrained conditions, misfit dislocations are less likely to form. Here we report a dislocation formation mechanism that would be unexpected from a continuum mechanics analysis. It was observed in molecular dynamics simulations of the vapor deposition of a lower-lattice-mismatch [NiFe/CoFe/Cu] multilayer system.

II. SIMULATION METHODOLOGY

Unlike the continuum assumption, a real crystal is composed of discrete atoms located at certain lattice sites. These atoms are held together by their interatomic interactions to form a solid crystal. If an adatom is deposited on a surface, it interacts with other atoms in the crystal. This interaction then defines an array of sites on the surface that gives either global or local minimum for the total energy of the system. These sites define new lattice sites. During vapor deposition, however, some of the local-energy-minimizing sites may not belong to the perfect lattice and are defective sites. Upon deposition, adatoms can occupy either lattice or defective sites, although defective sites usually become energetically unfavorable as additional atoms are deposited. Atom vibration allows atoms to jump from one site to another through thermal activation. The jump frequency depends on temperature and the energy barrier along the jump path. Typically, the energy barriers along the jump paths on the surface are smaller than those in the bulk. As a result, surface atoms are much more mobile than bulk atoms. The atomic structure obtained during deposition is then a result of a combination of which sites the adatoms initially land on and how surface atoms jump before they are buried into the bulk by later deposited atoms. The deposition rate contributes to the structure evolution because it determines the time available for atoms to jump while located on the surface. Because many surface jump paths with different activation barriers are encountered, and the population of such paths depends upon the local atomic configuration, the atomic assembly during deposition is a very complicated process to understand.[34]

Defects can be easily formed during deposition. For instance, a surface asperity can create incident atom flux shadow on the surface, promoting the formation of surface roughness and voids when other surface atoms are not mobile enough to migrate to the shadowed regions.[30] If atoms that are initially deposited into the defective sites are buried within the bulk before they can hop out of these sites, various defects can form, including twins, dislocations, and grain boundaries. The energy carried by the incident adatoms can assist structure modification of the deposited films. For instance, the latent heat release during an atom's condensation together with dissipation of the remote kinetic energy of the adatom can both contribute to a local thermal spike on the surface during adatom impact.[31] This local thermal spike can induce ''extra'' local surface reconstruction, above that expected by purely thermal activation, and it can result in surface flattening and mixing of atoms across interfaces during the growth of multilayers.[32] High-energy adatoms impacting a smooth surface at an oblique angle can also skip on the surface for a long distance before come to rest.[31] Depending on the incident angle, hyperthermal energy adatoms can be reflected or cause resputtering.[33] A molecular dynamics (MD) simulation approach can realistically capture all the atomistic assembly processes described above and to provide accurate mechanisms for dislocation formation.

In MD, a real crystal is simulated. By defining the forces between atoms using an interatomic potential, and by assigning an initial velocity distribution to all the atoms based on the simulated temperature, Newton's equations of motion are then used to obtain positions of all atoms as a function of time. The results provide information about the atom vibration and atom jumping. For vapor deposition, the initial crystal is used as a substrate. Periodic boundary conditions are typically used for the two in-plane (growth surface) coordinate directions to minimize the effect of small length scales in these two directions. To simulate the free (growth) surface, a free boundary condition is used for the third coordinate direction. Vapor deposition can be simply simulated by continuously injecting adatoms toward one of the free surfaces of the crystal at a frequency determined by the deposition rate. Because MD simulations solve for atom vibrations, the time step must be less than the shortest lattice vibration period (typically around 10^{-15} s). Consequently, an accelerated rate of deposition is normally used in order to deposit enough atoms in the available computational time to reveal structural features. To prevent the simulated crystal from shifting due to the momentum transfer during adatom impact, several monolayers of atoms at the other free surface are fixed.

Newton's equation of motion preserves the total energy. The initial kinetic energy of hot adatoms together with their latent heat release during condensation then causes a continuous increase of temperature in the simulated crystal. To simulate an isothermal deposition like that encountered in

experiments, damping forces can be applied to atoms in a selected ''isothermal'' region below the surface.[32] The sign of the damping force is chosen to increase the atom velocities when the run time temperature is lower than the desired temperature. Otherwise it is chosen to reduce the atom velocities. This approach ensures that the atomistic events at the surface are purely determined by Newton's equation of motion, and the energy created at the free surface due to adatom impact is naturally conducted to the isothermal region, where it is dissipated. To provide a stable heat sink during accelerated rate deposition, the isothermal region can be propagated during simulation to keep pace with the movement of the surface (growth) front.

The accuracy of MD simulations critically depends on the interatomic potential. For studying dislocation formation in lattice-mismatched systems, the potentials must accurately predict lattice constants, elastic constants, cohesive energies, and the vacancy formation energies. One such potential is based upon the embedded atom method (EAM) originally developed by Daw and Baskes.[37] In addition to a pairwise energy term, the EAM efficiently incorporates the many-body dependence of the potentials by an embedding energy term. As a result, EAM potentials well describe the properties such as lattice and elastic constants, cohesive energies, and the vacancy formation energies of close-packed transition metals.

The EAM potential for a monatomic element is invariant to a transformation in which a term linear in the electron density is added or subtracted from the embedding energy function as long as an appropriate adjustment is made to the pairwise term.[38] Thus, the many monatomic EAM functions developed by different authors may appear different, but are in fact similar upon transformation. This additional freedom of elemental potentials, however, affects the predicted alloy properties when they are combined to study alloys.[38] This means that the monatomic potentials cannot be simply used to model alloys unless they are normalized to a unique state. By specifically fitting the parameters of the EAM potentials to alloy properties (such as the heat of solution), ''alloy'' EAM potentials have been devised for some alloys.[39–41] However, most of these alloy potentials are of restricted utility and cannot be simply combined with other published EAM potentials to study other alloys. A recently developed alloy EAM potential database of sufficient generality has enabled alloy potentials from as many as 16 metals (Cu, Ag, Au, Ni, Pd, Pt, Al, Pb, Fe, Mo, Ta, W, Mg, Co, Ti, and Zr) to be created from normalized elemental potentials.[42,43] This potential database was recently modified and is described in Appendix A. It has been successfully applied to simulate the deposition of a number of metal multilayer systems.[30,32,42] The MD simulations reported here utilized this set of alloy EAM potentials.

III. OBSERVATIONS OF DISLOCATION FORMATION

The MD simulation approach described above was used to investigate the growth of $(10\,\text{Å})Co_{90}Fe_{10}/(20\,\text{Å})Ni_{82}Fe_{18}/(20\,\text{Å})Co_{90}Fe_{10}$ on a (111) Cu substrate, Fig. 1. This multilayer structure is similar to the ones widely utilized in GMR structures.[44] The initial Cu substrate had 68 $(2\bar{2}0)$ planes in the x direction, three (111) planes in the y (growth) direction, and 24 $(\bar{2}\,\bar{2}4)$ planes in the z direction. To simplify observation of possible edge-type misfit dislocations, the x direction was chosen to be in line with the Burgers vector of a typical $[(a/2)\langle 110\rangle]$ unit dislocation in a fcc structure. A MD algorithm that allows the periodic lengths to change was used.

The simulations were performed at a substrate temperature of 300 K. The vapor atoms were injected perpendicular to the growth surface. The frequency of vapor atom addition corresponded to a growth rate of 10 nm/ns. Due to the computational expense of MD simulations, the simulated deposition time was limited to 500 ps. It should be noted that, although the resulting accelerated deposition rate reduces the time for defects to anneal out, the high flux of adatoms exaggerates the energy (temperature) accumulation at the free surface region. Recent analysis of this phenomenon indicated that the vibrationally excited surface is able to activate atomic jumps that would not have occurred in a purely isothermal environment,[31] and so the high deposition rate significantly accelerates the annealing of defects. This effect has also been utilized to develop accelerated molecular dynamics methods.[45,46] Exaggerated deposition rate and surface temperature to some degree compensate, and hence the MD algorithm used may be a reasonable approximation to lower-growth-rate conditions.

Various incident atom energies were explored. Figure 1 was obtained using a low (thermalized) adatom energy of 0.2 eV. In the figure, the blue, gray, pink, and orange balls represent Ni, Fe, Co, and Cu atoms, respectively. Dislocations are present in the structure, but they can be difficult to identify. To more clearly reveal these dislocations, two-dimensional atomic arrays were examined. Two regions marked ''1'' and ''2'' in Fig. 1 were selected for this analysis. All the x-y atomic planes in these two regions were projected into two-dimensional figures shown, respectively, in Figs. 2(a) and 3. Note that the colors are now used to distinguish different monolayers instead of different atom species. Figures 2(a) and 3 show the extensive edge (extra half plane) dislocations aligned parallel to the interface. Two dislocations are found near the CoFe-on-Cu interface (region 1). Two others are found five monolayers above the CoFe-on-Cu interface (region 2).

The nature of the dislocations observed in region 1 of Fig. 1 was further analyzed. Three adjacent (111) monolayers A, B, and C, colored with purple, red, and yellow, respectively, in Fig. 2(a), were viewed from the y (growth) direction. The (111) plan view of these three monolayers is presented in Fig. 2(b). By tracing purple atoms from left to right, it can be seen from Fig. 2(b) that they first undergo a shift from fcc to hcp sites at the location of the left dislocation shown in Fig. 2(a). They then undergo a shift from hcp to fcc sites at the position of the right dislocation in Fig. 2(a). This creates a stacking-faulted region bounded by fcc lattices at the left and right. The vectors for the two lattice shifts are identified as $(a/6)[1\bar{2}1]$ and $(a/6)[2\bar{1}\,\bar{1}]$ as shown in Fig. 2 (a is the lattice constant in this region). These two shifts result in two

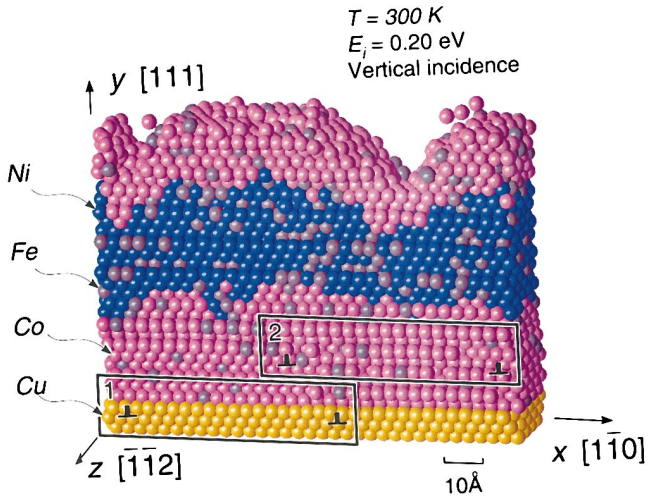

FIG. 1. (Color) Molecular dynamics simulated atomic configuration of a (10 Å)$Co_{90}Fe_{10}$/(20 Å)$Ni_{82}Fe_{18}$/(20 Å)$Co_{90}Fe_{10}$ multilayer deposited on a Cu substrate at a temperature of 300 K, a deposition energy of 0.20 eV, and a normal adatom incidence angle.

missing half $(2\bar{2}0)$ planes in the crystal above the red atoms, giving rise to a net Burgers vector of $(a/2)[1\bar{1}0]$. Hence, the two dislocations observed are partials, $(a/6)[1\bar{2}1]$ and $(a/6)[2\bar{1}\bar{1}]$. These two partials can be viewed as dissociated from a unit dislocation $(a/2)[1\bar{1}0]$.

Using atomistic simulation, Appendix B calculates the line energy of the $(a/6)\langle 112\rangle$ dislocation in nickel as a function of the depth of dislocation below the surface. The results are shown in Fig. 5 below. Figure 5 indicates that, as the

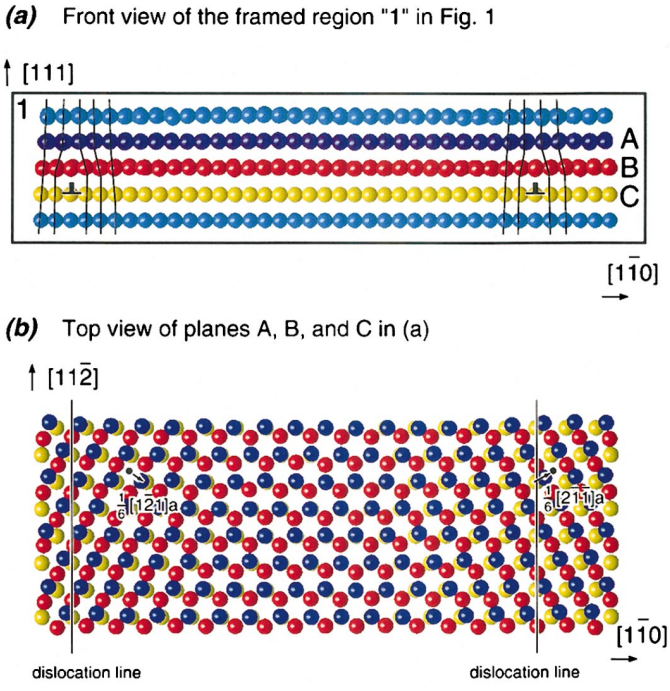

FIG. 2. (Color) Front and top views of region 1 of the crystal shown in Fig. 1. (a) The front view (z projection), and (b) the top view (y projection). Different colors refer to different planes.

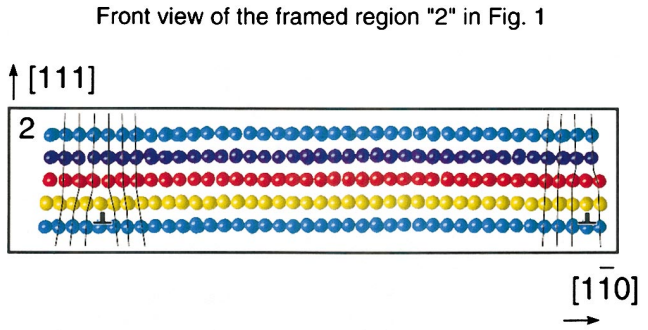

FIG. 3. (Color) A front view (z projection) of region 2 of the crystal shown in Fig. 1.

overlayer thickness increases, the dislocation line energy increases and quickly approaches a saturation value. The line energy is about 0.15 eV/Å when the dislocation is about one monolayer below the surface, and reaches about 0.4 eV/Å when the dislocation is about 10 monolayers (ML) below the surface.

To explore the effects of the incident atom energy upon the formation and retention of the dislocations shown in Figs. 2 and 3, the growth of the same multilayers was simulated using remote adatom kinetic energies from 0.1 to 5.0 eV. The results indicated that formation of these dislocations was sensitive to the adatom's kinetic energy. Dislocations were readily formed and retained for energies below 2.0 eV. However, no dislocations were observed when the incident atom energy was increased above 2.0 eV. Real films have much larger length scales than the simulated system. As a result, dislocations might still form at relatively high energies. Nevertheless, these results suggest that the density of such dislocations will be much lower under the high-energy deposition conditions encountered during, say, low-pressure magnetron or ion beam deposition.

IV. MISMATCH STRAIN ACCOMMODATION

Figures 2 and 3 indicate that during high-growth-rate, low-temperature deposition, edge-type dislocations with Burgers vector parallel to the interfaces are formed. At first sight, these dislocations appear similar to the misfit dislocations that accommodate lattice mismatch. However, further analysis indicated otherwise. The edge dislocations in Figs. 2 and 3 are marked by missing $(2\bar{2}0)$ planes in the $Co_{90}Fe_{90}$ layer with respect to the copper substrate. This is interesting because copper atoms are bigger than the cobalt, nickel, or iron atoms that are in the layer deposited on the copper. As a result, the opposite [extra $(2\bar{2}0)$ planes] would have been expected from misfit dislocation considerations. We are unaware of previous reports of this kind of dislocation structure in this system. We have analyzed this dislocation structure further to better understand why it is formed.

Ideal bulk crystals were created for fcc copper, cobalt, and nickel (pure iron is not considered here since its bcc structure would complicate the analysis) by imposing periodic boundary conditions in all coordinate directions. A conjugate gradient method was then utilized to relax the periodic lengths

TABLE I. Relaxation of Cu crystal due to surface effects.

	Lattice constant (Å)	Interplane spacing (Å)			Percentage change (%)		
	a	$d_{(\bar{2}\,\bar{2}4)}$	$d_{(22\bar{0})}$	$d_{(111)}$	$\varepsilon_{(\bar{2}\,\bar{2}4)}$	$\varepsilon_{(22\bar{0})}$	$\varepsilon_{(111)}$
Bulk values	3.615	0.738	1.278	2.087			
3 ML Cu substrate		0.732	1.269	2.096	−0.81	−0.70	0.43

and find the equilibrium positions of all the atoms. From these calculations, we obtain the lattice constants for copper, cobalt, and nickel crystals as 3.615, 3.549, and 3.520 Å, respectively. The percentage size differentials of cobalt and nickel with respect to copper are −1.826% and −2.628%, respectively. These negative size differentials cause tensile stress in epitaxially deposited cobalt or nickel layers and compressive stress in the copper substrate. Any missing planes in either the cobalt- or nickel-rich layers with respect to the copper layer increase this stress.

It is well known that the lattice parameter of a metal surface can be smaller than that of the bulk due to the effect of surface tension. One possibility for the appearance of the dislocation in Figs. 2 and 3 is that the surface lattice parameter of copper becomes smaller than that of the ferromagnetic layer deposited on to it. To explore this possibility, a conjugate gradient method was used to calculate the equilibrium lattice constant of a three-(111)-monolayer copper crystal. The plane spacing in the three coordinate directions for both the 3 ML copper crystal and bulk copper, together with the percentage changes of plane spacing of the 3 ML crystal with respect to those of the bulk crystal, are listed in Table I.

Table I indicates that because of free surface effects the copper lattice shrinks in the in-plane $[1\bar{1}0]$ and $[\bar{1}\,\bar{1}2]$ directions. These shrinkages cause a slight expansion in the third [111] direction. Even using the plane spacing $d_{(\bar{2}\bar{2}4)}$ which shrinks the most, the reduced lattice constant of 3.59 Å remains greater than the bulk lattice constants of both cobalt and nickel. It must be concluded that free surface effects alone cannot account for the observed dislocation formation.

To further explore the mismatch between the copper substrate and the deposited multilayer, we separated the deposited multilayer from the substrate. A conjugate gradient method was used to calculate the equilibrium crystal size of the stand-alone multilayer $Co_{90}Fe_{10}/Ni_{82}Fe_{18}/Co_{90}Fe_{10}$, the stand-alone copper substrate, and the joined system consisting of both the substrate and the multilayer $Co_{90}Fe_{10}/Ni_{82}Fe_{18}/Co_{90}Fe_{10}/Cu$. The strains (as described in Appendix C) were then calculated. The results of these calculations are compared in Table II. They indicate that the deposited multilayer must undergo overall positive strains γ of 0.09% in the x direction and 0.67% in the z direction to form the joined structure shown in Fig. 1. They also show that the free-standing copper substrate must undergo a negative strain of −5.01% in the x direction and −1.54% in the z direction to form the joined structure.

One can also look at the mismatch between an ideally flat cobalt layer deposited on an ideally flat copper substrate with similar interfacial dislocations. We can assume that cobalt is relatively thicker than copper to mimic the simulated case. Because the cobalt layer is thick, it should have a negligible change in size when it is joined with the thin copper layer. This means that the cobalt layer retains the equilibrium size of the fcc bulk cobalt after it is joined with the copper layer. Using this as an approximation, the epitaxial strain of copper defined with respect to the equilibrium fcc bulk copper lattice constant can be directly calculated from the lattice constants. For the same two partial dislocations distributed over the same length scale in the x direction as shown in Fig. 1, there are 68 $(2\bar{2}0)$ planes in the copper substrate and 66 $(2\bar{2}0)$ planes in the cobalt layer. The copper strain in the x direction is then $(66a_{Co}/a_{Cu}-68)/68\approx -4.7\%$. This is close to the strain in the x direction listed in Table II.

The analyses discussed above verify that the internal strains between the substrate and the deposited layers are essentially correctly represented in the simulations. The observed dislocations therefore do increase the mismatch strain during the deposition of the smaller-lattice-parameter cobalt or nickel layers on a copper substrate. Unlike the misfit dislocations discussed in continuum theories[8,12] or in the atomistic simulation of a larger-lattice-mismatch system such as $Au/Ni_{0.8}Fe_{0.2}$,[35] the dislocations observed here are not equilibrium configurations. This is consistent with the finding that the dislocation density decreases at high deposition energies which promote equilibrium.

If missing planes are formed during deposition of smaller atoms on a surface composed of larger atoms, then they should more easily form during deposition of bigger atoms

TABLE II. Crystal size calculations.

Crystal	Length in x direction (Å)	Length in z direction (Å)	γ_x (%)	γ_z (%)
$Co_{90}Fe_{10}/Ni_{82}Fe_{18}/Co_{90}Fe_{10}$	81.880	17.185	0.09	0.67
Cu	86.272	17.570	−5.01	−1.54
$Co_{90}Fe_{10}/Ni_{82}Fe_{18}/Co_{90}Fe_{10}/Cu$	81.953	17.300		

on a surface composed of smaller atoms. Numerous simulations were carried out to deposit Cu on a (111) Co substrate under similar kinetic conditions. As anticipated, a higher density of dislocations was observed. In this case, the dislocations were the conventional ''misfit'' dislocations.

V. DISLOCATION FORMATION MECHANISMS

To explore how the observed dislocations are created, we have analyzed the atomic scale structures intermittently during the growth process, Figs. 4(a)–4(d). Figure 4 shows side (*z*) and top (*y*) projection views of a (10 Å)$Co_{90}Fe_{10}$/(20 Å)$Ni_{82}Fe_{18}$/(20 Å)$Co_{90}Fe_{10}$ multilayer deposited with an adatom energy of 0.2 eV. The *z*-projected image in Fig. 4(d) reveals a dislocation (an extra half plane). Three different colors are used to mark three adjacent (111) planes. The plane above the dislocation is colored purple, the plane below the dislocation is colored yellow, and the plane through the dislocation is colored red. The *y*-projected image can then be used to show the in-plane configurations of these three planes. Similar observations are illustrated in Figs. 4(a)–4(c) where the planes are shown at earlier stages of the deposition.

If the film had grown as a perfect fcc structure with an *ABCABC*... (111) stacking sequence, the atoms of any three adjacent planes should all be visible when viewed from the [111] (*y*) direction. At deposition time $t=46$ ps, Fig. 4(a), it can be seen from the *y*-projected image that the (111) planes have evolved to consist of three distinct regions. In the first region, all three different color atoms can be observed, consistent with a local fcc (*ABCABC*...) stacking sequence. In the second region, only purple and red atoms can be observed, indicative of local hcp (*ABAB*...) stacking. In the third region, no purple or red atoms can be observed, simply revealing that these domains have not yet been completely filled with atoms. At $t=86$ ps, Fig. 4(b), all the three planes have been almost filled. This leaves the (111) planes occupied by either fcc or hcp domains. With the further elapse of time to $t=111$ ps, Fig. 4(c), the boundaries between the fcc and the hcp domains appear to nucleate a missing $(2\bar{2}0)$ plane. Finally, at $t=186$ ps in Fig. 4(d), the missing plane representing a dislocation becomes clear in the *z*-projected image, and its horizontal location coincides exactly with the boundary between the fcc and the hcp domains. Comparing Figs. 4(c) and 4(d) indicates that such dislocations are highly mobile on the (111) slip plane, as a significant lateral shift of dislocation location occurred within a very short period of time (75 ps).

The nucleation of the observed dislocations that are parallel to the surface would increase the mismatch energy between the layers of $Co_{90}Fe_{10}$ and copper. It is interesting to understand why this occurred. It is noted that individual depositing atoms suffered only a small energy penalty when they occupied the wrong sites (i.e., hcp instead of fcc, or vice versa). For example, the binding energies of a single copper atom on the fcc and hcp sites of a (111) copper surface differ only by 0.002 eV.[47] As a result, there is a high probability of forming different stacking-fault domains during the growth

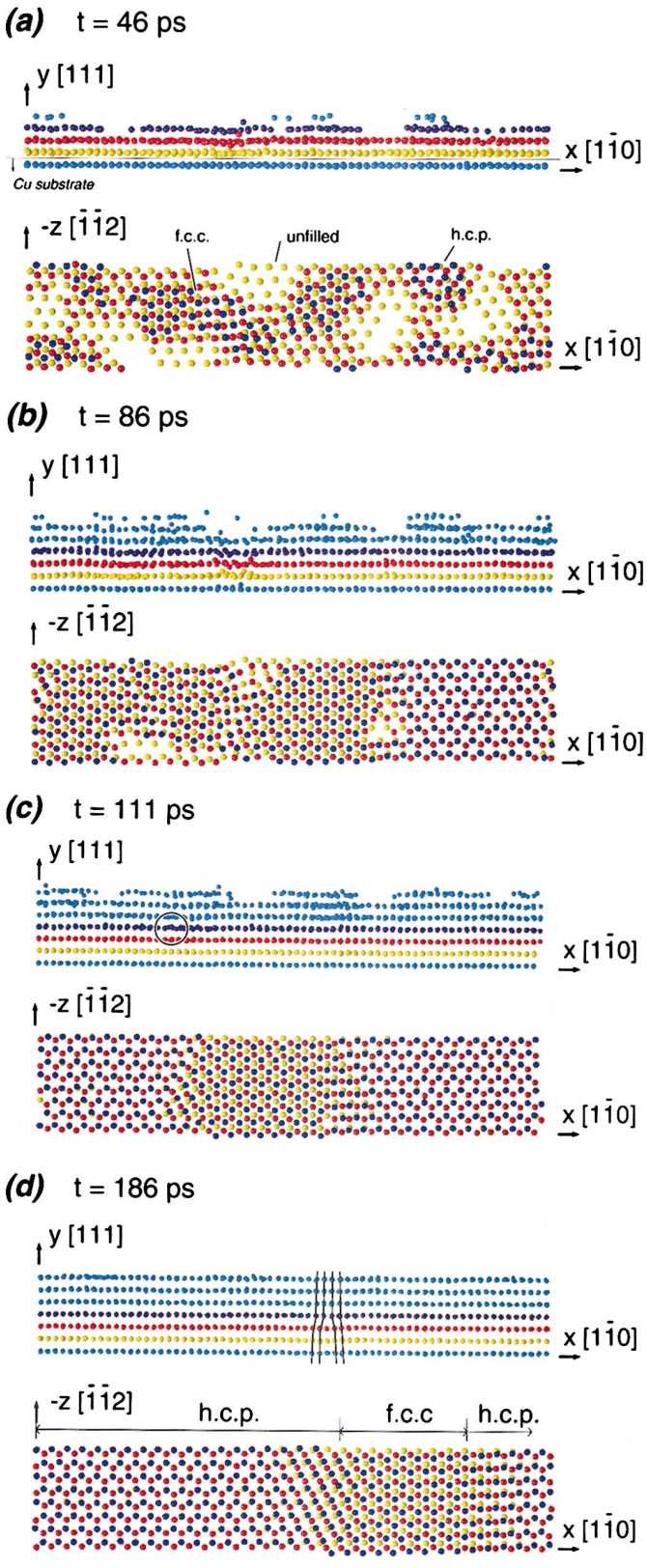

FIG. 4. (Color) Front and top views of the time-evolving atomic configuration of a (10 Å)$Co_{90}Fe_{10}$/(20 Å)$Ni_{82}Fe_{18}$/(20 Å)$Co_{90}Fe_{10}$ multilayer deposited on a Cu substrate at a temperature of 300 K, a deposition energy of 0.20 eV, and a normal adatom incidence. Time (a) 46, (b) 86, (c) 111, and (d) 186 ps.

of a CoFe (or NiFe) layer on the (111) surface of a fcc lattice. When the lateral boundaries (normal to the surface) of these fault domains meet, dislocations can be nucleated on the surface. While these dislocations may have high energies and are likely to be unstable, it requires the overcoming of a relatively higher energy barrier for them to anneal out. As a result, kinetically constrained atomic assembly can result in the direct nucleation of dislocations on the growth surface. Unlike the threading dislocation model,[8] these dislocations may form without preexisting threading dislocations.

The observations above explain why missing planes tend to occur in later deposited layers even though their lattice parameters are slightly smaller. Dislocations are nucleated by the contact of stacking fault/unfaulted domain boundaries. These domain boundaries have either extra planes or missing planes. However, since these boundaries are filled last during each layer growth, it is likely that they cannot be completely filled, resulting in missing planes, at least at the initial contact of domain boundaries. If the growth rate is low so that these boundaries are at the surface, the filling of the missing planes would require squeezing of extra rows of atoms into these locations in the top surface monolayer. This is energetically unfavorable, at least locally, because the local compressive strain energy caused by the discrete lattice will then be significantly larger than the global misfit strain energy, which is very small for a thin film thickness. If the growth rate is high enough so that the junctions of these domain boundaries are buried below the surface, then the filling of these places would require atoms to diffuse into these regions. These events are associated with significant activation energy barriers and less frequently occur under kinetically constrained growth conditions. As a result, edge dislocations with missing planes in the later deposited layers with respect to previously deposited layers are a natural product of the atomic assembly process during epitaxial deposition of the (111) surface of fcc multilayer lattices.

Under conditions that promote equilibrium, such as increasing deposition energy or substrate temperature, or reducing deposition rate, the combination of impact-energy-induced and thermally activated diffusion events can proceed sufficiently to anneal out defects. This explains why no dislocations were observed in similar simulations performed using adatom kinetic energies above 2.0 eV.

VI. CONCLUSIONS

Molecular dynamics simulations of vapor deposition of a CoFe/NiFe/CoFe/Cu multilayer system revealed the following.

(a) Edge dislocations can form along the interfaces under kinetically constrained growth conditions. These dislocations tend to have missing planes in the later deposited layer with respect to the earlier deposited layer. Therefore, they can either relieve or increase the misfit strain energy. The dislocations in the latter case differ from traditional ''misfit'' dislocations and are a manifestation of the highly nonequilibrium growth environment.

(b) The misfit-energy-*increasing* dislocations are found to form directly on the surface. During the growth on the (111) surface of a fcc lattice, adatoms may either occupy fcc or hcp sites. This results in the formation of fcc and hcp domains on surface. The dislocations are a natural product of the joining of these domain boundaries. The missing planes in the later deposited layer simply resulted from the incomplete filling of these domain boundary regions under kinetically limited growth conditions.

(c) The use of conditions that promote atom diffusion, such as an increase of the deposition energy, greatly reduces the probability of forming the mismatch-*increasing* dislocations.

ACKNOWLEDGMENT

We are grateful to the Defense Advanced Research Projects Agency (D. Healy and S. Wolf, Program Managers) for support of this work.

APPENDIX A: METAL ALLOY EMBEDDED ATOM METHOD POTENTIAL DATABASE

An integrated EAM potential database applicable to a number of metals and their alloys has been proposed.[42] This database has been modified and is briefly described here. In the EAM, the total energy E of the crystal can be expressed as

$$E=\frac{1}{2}\sum_{i,j,i\neq j}\phi_{ij}(r_{ij})+\sum_{i}F_i(\rho_i), \tag{A1}$$

where ϕ_{ij} represents the pair energy between atoms i and j separated by a distance r_{ij}, and F_i is the embedding energy associated with embedding an atom i into a local site with an electron density ρ_i. The electron density can be calculated using

$$\rho_i=\sum_{j,j\neq i}f_j(r_{ij}) \tag{A2}$$

with $f_j(r_{ij})$ the electron density at the site of atom i arising from atom j at a distance r_{ij} away.

For a pure element a, the EAM potential is composed of three functions: the pair energy ϕ, the electron density ρ, and the embedding energy F. For an alloy, the EAM potential contains not only the three functions ϕ, ρ, and F for each of the constituent elements, but also the pair energy ϕ_{ab} between different elements a and b $(a\neq b)$. In general, the published EAM potentials for atoms of a single element are based upon different reference states and inconsistent interaction cutoff distances. As a result, the functions ϕ, ρ, and F fitted for elemental metals cannot be directly applied to alloy or multilayer systems. However, by normalizing the EAM potentials and introducing an EAM alloy model,[38] a procedure to generalize the EAM potentials and their cutoff distance has been recently proposed.[42] This enables alloy EAM potentials to be constructed from elemental EAM potentials. Such alloy potentials have been used in MD simulations to produce results that are encouragingly seen in experiments.[42] In this EAM alloy potential model, the generalized elemental pair potentials are written

TABLE III. EAM parameters.

	Cu	Ag	Au	Ni	Pd	Pt	Al	Pb
r_e	2.556 162	2.891 814	2.885 034	2.488 746	2.750 897	2.771 916	2.863 924	3.499 723
f_e	1.554 485	1.106 232	1.529 021	2.007 018	1.595 417	2.336 509	1.403 115	0.647 872
ρ_e	21.175 871	14.604 100	19.991 632	27.562 015	21.335 246	33.367 564	20.418 205	8.450 154
ρ_s	21.175 395	14.604 144	19.991 509	27.930 410	21.940 073	35.205 357	23.195 740	8.450 063
α	8.127 620	9.132 010	9.516 052	8.383 453	8.697 397	7.105 782	6.613 165	9.121 799
β	4.334 731	4.870 405	5.075 228	4.471 175	4.638 612	3.789 750	3.527 021	5.212 457
A	0.396 620	0.277 758	0.229 762	0.429 046	0.406 763	0.556 398	0.134 873	0.161 219
B	0.548 085	0.419 611	0.356 666	0.633 531	0.598 880	0.696 037	0.365 551	0.236 884
κ	0.308 782	0.339 710	0.356 570	0.443 599	0.397 263	0.385 255	0.379 846	0.250 805
λ	0.756 515	0.750 758	0.748 798	0.820 658	0.754 799	0.770 510	0.759 692	0.764 955
F_{n0}	−2.170 269	−1.729 364	−2.937 772	−2.693 513	−2.321 006	−1.455 568	−2.807 602	−1.422 370
F_{n1}	−0.263 788	−0.255 882	−0.500 288	−0.076 445	−0.473 983	−2.149 952	−0.301 435	−0.210 107
F_{n2}	1.088 878	0.912 050	1.601 954	0.241 442	1.615 343	0.528 491	1.258 562	0.682 886
F_{n3}	−0.817 603	−0.561 432	−0.835 530	−2.375 626	−0.231 681	1.222 875	−1.247 604	−0.529 378
F_0	−2.19	−1.75	−2.98	−2.70	−2.36	−4.17	−2.83	−1.44
F_1	0	0	0	0	0	0	0	0
F_2	0.561 830	0.744 561	1.706 587	0.265 390	1.481 742	3.010 561	0.622 245	0.702 726
F_3	−2.100 595	−1.150 650	−1.134 778	−0.152 856	−1.675 615	−2.420 128	−2.488 244	−0.538 766
η	0.310 490	0.783 924	1.021 095	0.469 000	1.130 000	1.450 000	0.785 902	0.935 380
F_e	−2.186 568	−1.748 423	−2.978 815	−2.699 486	−2.352 753	−4.145 597	−2.824 528	−1.439 436
	Fe	Mo	Ta	W	Mg	Co	Ti	Zr
r_e	2.481 987	2.728 100	2.860 082	2.740 840	3.196 291	2.505 979	2.933 872	3.199 978
f_e	1.885 957	2.723 710	3.086 341	3.487 340	0.544 323	1.975 299	1.863 200	2.230 909
ρ_e	20.041 463	29.354 065	33.787 168	37.234 847	7.132 600	27.206 789	25.565 138	30.879 991
ρ_s	20.041 463	29.354 065	33.787 168	37.234 847	7.132 600	27.206 789	25.565 138	30.879 991
α	9.818 270	8.393 531	8.489 528	8.900 114	10.228 708	8.679 625	8.775 431	8.559 190
β	5.236 411	4.476 550	4.527 748	4.746 728	5.455 311	4.629 134	4.680 230	4.564 902
A	0.392 811	0.708 787	0.611 679	0.882 435	0.137 518	0.421 378	0.373 601	0.424 667
B	0.646 243	1.120 373	1.032 101	1.394 592	0.225 930	0.640 107	0.570 968	0.640 054
κ	0.170 306	0.137 640	0.176 977	0.139 209	0.5	0.5	0.5	0.5
λ	0.340 613	0.275 280	0.353 954	0.278 417	1.0	1.0	1.0	1.0
F_{n0}	−2.534 992	−3.692 913	−5.103 845	−4.946 281	−0.896 473	−2.541 799	−3.203 773	−4.485 793
F_{n1}	−0.059 605	−0.178 812	−0.405 524	−0.148 818	−0.044 291	−0.219 415	−0.198 262	−0.293 129
F_{n2}	0.193 065	0.380 450	1.112 997	0.365 057	0.162 232	0.733 381	0.683 779	0.990 148
F_{n3}	−2.282 322	−3.133 650	−3.585 325	−4.432 406	−0.689 950	−1.589 003	−2.321 732	−3.202 516
F_0	−2.54	−3.71	−5.14	−4.96	−0.90	−2.56	−3.22	−4.51
F_1	0	0	0	0	0	0	0	0
F_2	0.200 269	0.875 874	1.640 098	0.661 935	0.122 838	0.705 845	0.608 587	0.928 602
F_3	−0.148 770	0.776 222	0.221 375	0.348 147	−0.226 010	−0.687 140	−0.750 710	−0.981 870
η	0.391 750	0.790 879	0.848 843	−0.582 714	0.431 425	0.694 608	0.558 572	0.597 133
F_e	−2.539 945	−3.712 093	−5.141 526	−4.961 306	−0.899 702	−2.559 307	−3.219 176	−4.509 025

$$\phi(r)=\frac{A\exp[-\alpha(r/r_e-1)]}{1+(r/r_e-\kappa)^{20}}-\frac{B\exp[-\beta(r/r_e-1)]}{1+(r/r_e-\lambda)^{20}}, \tag{A3}$$

where r_e is the equilibrium spacing between nearest neighbors, A, B, α, and β are four adjustable parameters, and κ and λ are two additional parameters for the cutoff. The electron density function is taken with the same form as the attractive term in the pair potential with the same values of β and λ, i.e.,

$$f(r)=\frac{f_e\exp[-\beta(r/r_e-1)]}{1+(r/r_e-\lambda)^{20}}. \tag{A4}$$

The pair potential between different species a and b is then constructed as

$$\phi^{ab}(r)=\frac{1}{2}\left[\frac{f^b(r)}{f^a(r)}\phi^{aa}(r)+\frac{f^a(r)}{f^b(r)}\phi^{bb}(r)\right]. \tag{A5}$$

Embedding energy functions that work well over a wide range of electron density require that three equations be used

to separately fit three different electron density ranges. For a smooth variation of the embedding energy, these equations are required to match values and slopes at their junctions. These equations are

$$F(\rho)=\sum_{i=0}^{3} F_{ni}\left(\frac{\rho}{\rho_n}-1\right)^i, \quad \rho<\rho_n, \quad \rho_n=0.85\rho_e, \tag{A6}$$

$$F(\rho)=\sum_{i=0}^{3} F_i\left(\frac{\rho}{\rho_e}-1\right)^i, \quad \rho_n\leqslant\rho<\rho_0, \quad \rho_0=1.15\rho_e, \tag{A7}$$

$$F(\rho)=F_e\left[1-\ln\left(\frac{\rho}{\rho_s}\right)^{\eta}\right]\left(\frac{\rho}{\rho_s}\right)^{\eta}, \quad \rho_0\leqslant\rho. \tag{A8}$$

This generalized EAM potential has been extended to include 16 metals and their solutions. The parameters needed to define the EAM model for these metals are listed in Table III. These potentials are well fitted to basic material properties such as lattice constants, elastic constants, bulk moduli, vacancy formation energies, and sublimation energies, and they predict reasonably well the heats of solution. The recent development of this potential database has enabled the use of molecular dynamics for the simulation of a variety of multilayer assembly from alloy vapors such as the one reported here. Provided one is not dealing with metal compound formation, the potential provides a reasonable approximation to the interactions between different metal elements in metallic solutions.

APPENDIX B: ENERGETICS OF DISLOCATIONS

The simulations identified the existence of nonequilibrium edge dislocations. It is important to quantify the energy of these dislocations to better understand their formation. To be consistent with the continuum analysis, the mismatch strain energy and dislocation line energy need to be separated. This means that in atomistic simulation, the dislocation line energy can be calculated only for pure elements. Pure nickel was calculated.

The dislocation energy can be viewed as the extra energy of a crystal containing a dislocation with respect to a crystal without a dislocation. A $(a/2)\langle 110\rangle$ edge dislocations can be created in fcc computational crystals by inserting (or removing) two adjacent {220} planes in half of the crystal above the {111} slip plane.[48] After relaxing the crystal, the $(a/2)\langle 110\rangle$ dislocation naturally dissociates into two $(a/6)\langle 112\rangle$ Shockley partial dislocations bounding a stacking-fault ribbon on the {111} slip plane,[48] similar to the case observed here. While a free surface parallel to the slip plane can be used, periodic boundary conditions need to be used in the other two directions in order to calculate the dislocation energies. This is equivalent to simulating an array of dislocations aligning along the slip plane. Because the number of {220} planes above the slip plane is different from that below, there is a mismatch strain between the top and bottom parts of the crystal. This mismatch strain is a constant and will never vanish as the crystal thickness is increased. However, dislocations are linear defects and their strain field should vanish when the distance from the dislocation core is large. To resolve this problem, we used an alternative approach to create edge dislocations that allows accurate determination of dislocation energies.[35]

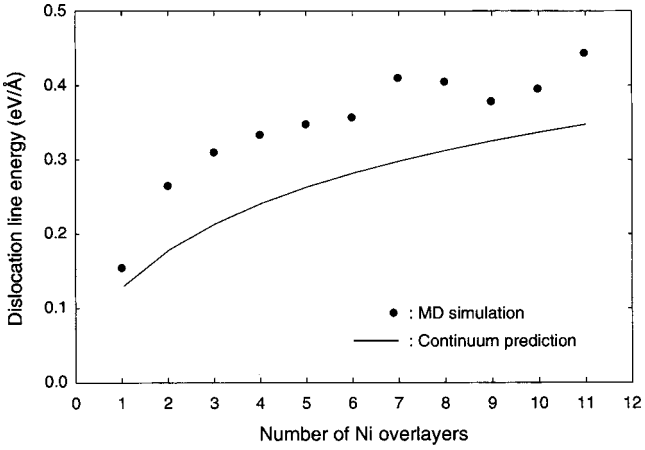

FIG. 5. Dislocation line energies as a function of number of deposited layers.

Assume that the energy of the relaxed crystals without dislocations and with a pair of partial dislocations are E_0 and E_d, respectively, the dislocation line energy for one $(a/6)\langle 112\rangle$ partial dislocation is

$$\Gamma=\frac{E_d-E_0-\sigma_{\mathrm{sf}}d\lambda_d}{2\lambda_d} \tag{B1}$$

where σ_{sf} is the stacking-fault energy, d is the separation between the two dislocations, and λ_d is the periodic length along the dislocation direction. A slab crystal with periodic boundary conditions in the in-plane directions and free surface boundary conditions in the thickness direction was used to calculate the stacking-fault energy. A stacking fault was created in the middle plane of the thickness by shifting the upper part with respect to the lower part by a vector of $(a/6)\langle 112\rangle$. The stacking-fault energy was calculated as the energy difference of the relaxed crystals with and without the stacking fault normalized by the total stacking-fault area. For nickel, we found $\sigma_{\mathrm{sf}}=0.0074\ \mathrm{eV/\AA^2}$. Since the thin film thickness lies in the dislocation core regime, the dependence of dislocation energy on film thickness needs to be addressed. This was achieved by studying crystals with different deposited layer thicknesses. The dislocation energy as a function of number of deposited monolayers is shown in Fig. 5.

In continuum theory, the edge dislocation has an energy of

$$E=\left[\frac{\mu b_e^2}{4\pi(1-\nu)}+\frac{\mu b_s^2}{4\pi}\right]\ln\left(\frac{h}{b}\right), \tag{B2}$$

where b, b_e, and b_s are, respectively, the total length, the edge component, and the screw component of the Burgers vector of the dislocation, ν is Poisson's ratio, μ is the shear modulus, and h is the deposited layer thickness. For n deposited (111) monolayers whose spacing is $d_{(111)}$, the film thickness $h=(n+1)d_{(111)}$. Using $\mu=0.5917\ \mathrm{eV/\AA^3}$ and ν

$=0.2529$, the dislocation line energy was calculated as a function of the number of deposited monolayers using Eq. (B2), and the results are included in Fig. 5. It is interesting to see that the continuum prediction is fairly close to that of the atomistic simulations. The atomistic simulations gave slightly higher results. It should be noted that continuum theories are based on an elastic anisotropic ratio of $A=1$, while a nickel single crystal has an anisotropic ratio of $A=2.5$. Dislocation core structures are also ignored in continuum models. Furthermore, continuum theories usually take the dislocation core radius at the unrealistically small value of b to try to account for the core energy. Both approximations are accurately treated in the atomistic simulations.

APPENDIX C: DEFINITION OF STRAINS

The strains discussed here refer to the normal strains created when individual free-standing layers are joined to form multilayers. Let the relaxed length of a given free-standing layer (either substrate or deposited layer) be $\lambda_{\alpha,f}$, and the length of the joined substrate/multilayer structure be $\lambda_{\alpha,j}$, where the first subscript $\alpha=1,2,3$ defines the three coordinate directions x, y, and z, and the second subscripts f and j mean the free-standing layer and joined structure, respectively. The strain in the α direction can be written as

$$\gamma_\alpha=\frac{\lambda_{\alpha,j}-\lambda_{\alpha,f}}{\lambda_{\alpha,f}}. \tag{C1}$$

[1] S. S. P. Parkin, Appl. Phys. Lett. **61**, 1358 (1992).
[2] S. Honda, S. Ohmoto, R. Imada, and M. Nawate, J. Magn. Magn. Mater. **126**, 419 (1993).
[3] S. S. P. Parkin, N. More, and K. P. Roche, Phys. Rev. Lett. **64**, 2304 (1990).
[4] J. C. S. Kools, J. Appl. Phys. **77**, 2993 (1995).
[5] H. N. G. Wadley, X. W. Zhou, and W. H. Butler, J. Phys. (France) (to be published).
[6] W. H. Butler, X. G. Zhang, D. M. C. Nicholson, and J. M. MacLaren, J. Magn. Magn. Mater. **151**, 354 (1995).
[7] D. M. C. Nicholson, W. H. Butler, X. G. Zhang, J. M. MacLaren, B. A. Gurney, and V. S. Speriosu, J. Appl. Phys. **76**, 6805 (1994).
[8] W. D. Nix, Metall. Trans. A **20**, 2217 (1989).
[9] B. Brar and D. Leonard, Appl. Phys. Lett. **66**, 463 (1995).
[10] H. Sato, M. Naito, S. Kinoshita, T. Arima, and Y. Tokura, Appl. Phys. Lett. **66**, 514 (1995).
[11] R. Ranjan, O. Buck, and R. B. Thompson, J. Appl. Phys. **61**, 3196 (1987).
[12] W. A. Jesser and J. Kui, Mater. Sci. Eng., A **164**, 101 (1993).
[13] J. P. Hirth, Acta Mater. **48**, 93 (2000).
[14] J. H. van der Merwe, J. Appl. Phys. **34**, 123 (1963).
[15] J. W. Matthews and A. E. Blakeslee, J. Cryst. Growth **27**, 118 (1974).
[16] J. W. Matthews and A. E. Blakeslee, J. Cryst. Growth **29**, 273 (1975).
[17] J. W. Matthews, J. Vac. Sci. Technol. **12**, 126 (1975).
[18] T. J. Gosling, S. C. Jain, J. R. Willis, A. Atkinson, and R. Bullough, Philos. Mag. A **66**, 119 (1992).
[19] S. C. Jain, T. J. Gosling, J. R. Willis, D. H. J. Totterdell, and R. Bullough, Philos. Mag. A **65**, 1151 (1992).
[20] S. R. Stiffler, C. L. Stanis, M. S. Gorsky, and K. K. Chan, J. Appl. Phys. **71**, 4814 (1992).
[21] S. R. Stiffler, C. L. Stanis, M. S. Gorsky, K. K. Chan, and E. de Fresart, J. Appl. Phys. **71**, 4820 (1992).
[22] J. W. Matthews, S. Mader, and T. B. Light, J. Appl. Phys. **41**, 3800 (1970).
[23] B. W. Dodson and J. T. Tsao, Appl. Phys. Lett. **51**, 1325 (1987).
[24] H. Steihardt and S. Schafer, Acta Metall. **19**, 65 (1971).
[25] H. Steihardt and P. Haasen, Phys. Status Solidi A **49**, 93 (1978).
[26] J. W. Matthews and A. E. Blakeslee, J. Cryst. Growth **32**, 265 (1976).
[27] C. S. Hartley, Scr. Metall. **3**, 607 (1969).
[28] X. W. Zhou, R. A. Johnson, and H. N. G. Wadley, Acta Mater. **45**, 4441 (1997).
[29] B. Lu, T. Klemmer, K. Wierman, G. Ju, D. Weller, A. G. Roy, D. E. Laughlin, C. Chang, and R. Ranjan, J. Appl. Phys. **91**, 8025 (2002).
[30] X. W. Zhou and H. N. G. Wadley, J. Appl. Phys. **87**, 553 (2000).
[31] X. W. Zhou and H. N. G. Wadley, Surf. Sci. **431**, 42 (1999).
[32] X. W. Zhou and H. N. G. Wadley, J. Appl. Phys. **84**, 2301 (1998).
[33] X. W. Zhou and H. N. G. Wadley, Surf. Sci. **431**, 58 (1999).
[34] Y. Yang, R. A. Johnson, and H. N. G. Wadley, Acta Mater. **45**, 1455 (1997).
[35] X. W. Zhou and H. N. G. Wadley, Philos. Mag. **84**, 193 (2004).
[36] F. M. Ross, K. M. Krishnan, N. Thangaraj, R. F. C. Farrow, R. F. Marks, A. Cebollada, S. S. P. Parkin, M. F. Toney, M. Huffman, C. A. Paz De Araujo, L. D. McMillan, J. Cuchiaro, M. C. Scott, C. Echer, F. Ponce, M. A. O'Keefe, and E. C. Nelson, MRS Bull. **21**(5), 17 (1996).
[37] M. S. Daw and M. I. Baskes, Phys. Rev. B **29**, 6443 (1984).
[38] R. A. Johnson, Phys. Rev. B **39**, 12 554 (1989).
[39] S. M. Foiles, Phys. Rev. B **32**, 7685 (1985).
[40] M. Asta and S. M. Foiles, Phys. Rev. B **53**, 2389 (1996).
[41] S. M. Foiles, M. I. Baskes, and M. S. Daw, Phys. Rev. B **33**, 7983 (1986).
[42] X. W. Zhou, H. N. G. Wadley, R. A. Johnson, D. J. Larson, N. Tabat, A. Cerezo, A. K. Petford-Long, G. D. W. Smith, P. H. Clifton, R. L. Martens, and T. F. Kelly, Acta Mater. **49**, 4005 (2001).
[43] H. N. G. Wadley, X. Zhou, R. A. Johnson, and M. Neurock, Prog. Mater. Sci. **46**, 329 (2001).
[44] T. C. Anthony, J. A. Brug, and S. Zhang, IEEE Trans. Magn. **30**, 3819 (1994).
[45] A. F. Voter, Phys. Rev. Lett. **78**, 3908 (1997).
[46] J. A. Sprague, F. Montaleni, B. P. Uberuaga, J. D. Kress, and A. F. Voter, Phys. Rev. B **66**, 205415 (2002).
[47] X. W. Zhou and H. N. G. Wadley, Acta Mater. **47**, 1063 (1999).
[48] J. von Boehm and R. M. Nieminen, Phys. Rev. B **53**, 8956 (1996).